2d infrared imaging at different wavelengths to characterize cycle-to-cycle variation of the combustion process in a Diesel engine

E. Mancaruso, L. Sequino, B.M. Vaglieco

Istituto Motori CNR, Napoli, Italy
*corresponding author: l.sequino@im.cnr.it

Abstract The internal combustion engine is the most common motor used for civil and commercial transportation even if it is a technology more than one century old. In order to update the engine, the most advanced diagnostics have been applied to investigate directly within the engine the processes that regulate its operation. Among these diagnostics, infrared cameras have taken a big technological leap in combustion research. While the typical techniques used for the visualization of liquid/vapor fuel, flames and burned gases are characterized by complex optical setup and the use of laser, the infrared diagnostic can be performed easily and can be effective as well.

In this work, both a visible and an infrared cycle resolved cameras have been used to visualize the phenomena that take place inside the cylinder of a compression ignition research engine fuelled with diesel fuel. The engine head is placed on an elongated cylinder and an optical access in the piston head provides the bottom view of the combustion chamber. The engine runs a multi-injection strategy typical of an operating point of the New European Driving Cycle. In order to interpret the different processes that occur at the same instant, three kinds of images have been recorded in the infrared spectrum. The first band analyzed is from 1.5 to 5 μm that is the camera range. A band pass filter at 4.2 μm has been used to impress the radiation of the CO_2 molecules. In addition, a filter at 3.9 μm has been applied to visualize the hydrocarbons distribution during the injection process.

The comparative analyses of the images recoded in the visible and infrared range, with and without band pass filters, has allowed to identify the presence of different processes at the same time. For example, during the main injection the fuel is delivered in a mix of fresh air, recirculated gas and reacting spray from the previous injection. Moreover, the availability of a cycle resolved infrared camera has allowed to investigate the engine cycle-to-cycle variation in terms of infrared emitted radiation and to compare it to the results of visible imaging. The data dispersion has been evaluated both in temporal and spatial location. It is the first time that this analysis is performed inside the combustion chamber of an engine. It denoted that the infrared imaging is suitable for this kind of applications. The better knowledge of in-cylinder processes is a powerful tool to control the combustion and to make the internal combustion engine more efficient.

Keywords: Diesel combustion, 2d infrared imaging, cycle-to-cycle variation

1 Introduction

Internal combustion engines (ICEs) are the most common motor for civil and commercial transport, and they have been strongly improved in the last years in order to reduce pollutant emissions and fuel consumption. Even if complex technologies are used to control the processes involved in the ICEs, further implementations are still needed. For example, optical diagnostics provided considerable insight for the development of modern engines. High temporal and spatial resolution and the non-intrusive character are the main advantages of these techniques. Several optical methods have been adopted in order to investigate all the steps of the functioning chain of ICE [1]. The visualization of the spray injection is typically performed by means of Mie scattering, Schlieren, and shadowgraph techniques [2] [3]. For the analysis of the species formed during the combustion process, optical techniques like emission spectroscopy in the UV-visible range, Laser Induced Incandescence, chemiluminescence, Laser Induced Fluorescence, and Raman are used [1] [4]. However, beside these techniques, further methods can be developed to gain additional insights into the combustion process. The investigation of the infrared (IR) spectrum has been performed mainly by means of spectroscopic emission [5] [6]. On the other hand, two-dimensional (2d) imaging in the infrared range has been used in the automotive sector to measure the temperature of the cylinder inner surface [7], to monitor the preheating plugs in diesel engines [8], to detect the brake thermal conditions [9], and to visualize the exhaust flow in catalytic converters [10]. However, 2d infrared imaging is still not very common for the investigation of high speed phenomena as those of ICEs. In [11], authors set up an IR camera to analyze the combustion process in an optically accessible diesel engine. They noted that the radiation emitted in this spectral range could be detected for a longer period than visible flame luminosity giving relevant insight about gas motion during the exhaust stroke. The hot gases above the piston head were visualized through the cylinder liner while a filter at the wavelength of 4.2 µm provided images of the carbon dioxide (CO_2) distribution from the bottom view. Further investigations were made in [12], commercial diesel fuel was compared with two biofuels of first and second generation. In [13], in addition to previous results, authors used a band pass filters at 3.9 µm in order to isolate liquid and reacting spray from hot gas.

In this work, 2d infrared imaging is performed in order to analyze more accurately the mixing process in a diesel engine. For the acquisition of in-cylinder images two high speed cycle resolved cameras have been used, one for the visible and one for the IR spectrum. The infrared range investigated is from 1.5 to 5 µm; moreover a band pass filter at 4.2 µm has been used to impress the radiation of the CO_2 molecules [14] while the C-H stretching bond has been detected using a filter at 3.9 µm [15]. The optical engine mounts the head of a real Euro5 diesel engine and a Common Rail injection system with solenoid injector. The engine head is placed on an elongated cylinder and an optical access in the piston provides the bottom view of the combustion chamber. Images are taken by means of a 45° IR-visible mirror located in the elongated piston. The engine has been run in continuous mode and performed a real operating condition of the New European Driving Cycle characterized by a double injection strategy. Comparison between cycle resolved visible and infrared images has never been performed previously, in particular inside an optical engine in continuous combustion mode. Infrared imaging has proven to give important information about the in-cylinder reactions, the CO_2 and fuel spatial distribution, and the cycle-to-cycle variation.

2 Experimental apparatus and procedures

OPTICAL ENGINE

The optical single-cylinder engine used for combustion diagnostics was equipped with the combustion system architecture and injection system of a Euro5 compliant four cylinders engine. The single-cylinder engine lay-out is shown in Figure 1. Moreover, the engine specifications are reported in Table 1. The optical engine utilized a conventionally extended piston with a piston crown window of 46 mm diameter which provided full view of the combustion bowl by locating an appropriate 45° fixed IR-visible mirror inside the extended piston. Even if the bowl bottom is flat, the combustion bowl volume and the bowl wall shape were kept the same as the production engine by reducing the bowl bottom distance. The window was made of sapphire to minimize the heat release differences between metal and optical engine [16]. To match the in-cylinder conditions of the multi-cylinder engine tests, an external air compressor was used to supply pressurized intake air that was filtered and dehumidified. Thanks to the dehumidification, the measure of the air mass flow, depending on the volume flow, the pressure and the temperature, is not affected by the uncertainties related to the presence of water. Then, the air was heated up to a desired inlet temperature that ensures the same rate of heat release of the metal engine [16, 17]. A reliable measure of the air mass flow before the mixing with the recirculated gases allows calculating the effective recirculation of exhaust gases (EGR) percentage. The engine was also equipped with a Common Rail injection system managed by a fully opened electronic control unit (ECU). A solenoid driven injector was used, more specifications about the injection system have been reported in Table 2. To analyze the current profile, a Hall-effect sensor was applied to the line of the solenoid of the injection. Moreover, to record the in-cylinder pressure in motored and fired condition, a piezoelectric pressure transducer (AVL GH13P) was set in the glow plug seat of the engine head. The cylinder pressure and the signal of the drive injector current were digitized and recorded at 0.1 crank angle degree (°CA) increments and ensemble-averaged over 150 consecutive combustion cycles. Moreover, the cyclic variation was measured and it resulted less than 1% with respect to the maximum pressure and less than 3% with respect to the indicated mean effective pressure (IMEP). The heat release rate was calculated from the ensemble-averaged pressure data using the first law of thermodynamics and the perfect gas model [18].

Table 1 Optical engine characteristics

Engine type	4-stroke single cylinder
Bore	85 mm
Stroke	92 mm
Swept volume	522 cm^3
Combustion bowl	19.7 cm^3
Vol. compression ratio	16.5:1

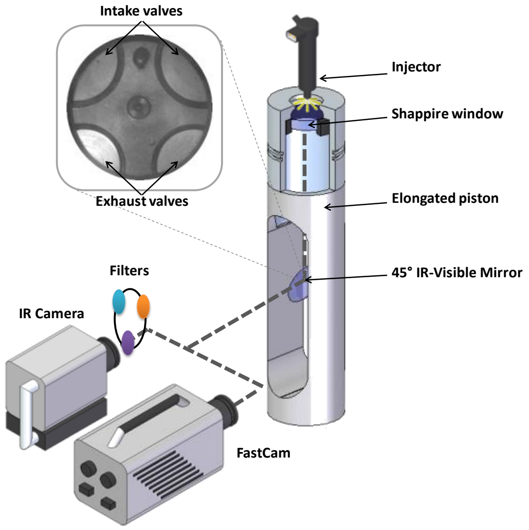

Fig. 1 Single-cylinder engine optical setup

Table 2 Injection system characteristics

Injection system	Common Rail
Injector type	Solenoid driven
Number of holes	7
Spreading angle of fuel jet axis	148°
Hole diameter [µm]	141

OPTICAL SETUP

Visible

In Figure 1, a scheme of the optical setup has been reported. Visible imaging analysis was performed by a cycle resolved Complementary Metal-Oxide Semiconductor (CMOS) camera through the 45° mirror. The camera is the FastCam SA-X2; it has a high sensitivity over a wide visible range and the pixel dimension is of 20 µm. A visible lens, Nikkor 50 mm f/2.8, was mounted. The f/stop used was f/22, the image size was 512x512 with a resolution of 0.17 mm per pixel, the image frequency was 30000 fps (one image each 0.4°CA at 2000 rpm) and the exposure time was 10 µs. The synchronization of the camera with the engine was obtained by a delay unit connected to the engine shaft encoder. For a statistical analysis of the spray and flames behavior 9 repetitions were performed.

Infrared

IR imaging was performed using the FLIR Phoenix fast camera able to detect light in the range 1.5-5 µm. The IR camera had a sensor made of Indium Antimonide and it was equipped with a 25 mm lens, f/2.3. The cycle resolved camera was used at 6000 fps that corresponds to an angular step of 2°CA at 2000 rpm. In order to obtain this temporal resolution, only half view of the camera has been selected. The size of the images was 128x24 pixels with a resolution of 1.1 mm per pixel. Images from IR camera were detected with an exposure time of 10 µs. However, it was necessary to use a Neutral Density filter with 10% attenuation

(ND1) to prevent the saturation of the detected images during the combustion.

The spectral range of the IR camera is quite wide (1.5-5 μm). Several species related to the combustion process emit in this band, e.g. CO, CO2, CH, OH, H2O et al. [15]. Beside the collection of the IR emission in the whole camera range, two band pass filters have been selected to visualize single chemical species. Since the asymmetric stretch vibrational mode of the CO_2 molecules correspond to wavelength 4.2 μm [14], a band pass filter at this wavelength has been used to visualize the in-cylinder distribution of CO_2. The second band pass filter used is at the wavelength 3.9 μm. This is affected by the presence of species whose signal is centered close to this wavelength. For example, the OH peaks due to carboxylic acids (COOH), the alkyl C-H and the aldehyde C-H [15]. Hence, the band pass filter at 3.9 μm has been used to visualize the hydrocarbons (HCs) and the intermediate products of the combustion reactions. The bandwidth of both filters is ± 150 nm.

ENGINE OPERATING CONDITION

The data presented in this paper were taken with the optical engine operating in continuous mode and true recirculation of exhaust gases (EGR) was performed using the hot gases of each combustion cycle. The EGR is used in order to reduce the emission of nitrogen oxides (NOx) and it was set to 29%. The engine operating condition investigated was representative of the engine behavior installed on a D-class vehicle during the New European Driving Cycle (NEDC). It corresponded to the calibration points at 2000 rpm at 5 bar of brake mean effective pressure (BMEP). In motored conditions, temperature and density at Top Dead Center (TDC) were estimated assuming the pressure at the bottom dead center (BDC) equal to the intake manifold pressure and a polytropic transformation with a coefficient of 1.36 [18]. This value was chosen after a validation procedure considering a sample of motored data at different intake pressures and engine speeds.

Table 3 Fuel properties

Feature/Method	**Units**	**Commercial Diesel**
Density @ 15 °C (EN ISO 12185)	*[kg/m^3]*	829
Cetane Number (EN ISO 5165)	*[-]*	51.8
Low Heating Value (ASTM D3338)	*[MJ/kg]*	42.4
Flash Point (ASTM D93/IP 34/ EN ISO 2719)	*[°C]*	72
Kinematic Viscosity 40°C (ASTM D445)	*[mm^2/s]*	2.7
Cloud Point (ASTM D2500)	*[°C]*	-2.2
Cold Filter Plugging Point (EN 116)	*[°C]*	-19
Lubricity 60°C (ISO 12156-1)	*[μm]*	382
Distillation (ASTM D86)	*IBP [°C]*	159
	10%vol. [°C]	194
	50%vol. [°C]	268
	90%vol. [°C]	333
	95%vol. [°C]	350
	FBP [°C]	361
Carbon (ASTM D5991)	*[mol%]*	~85.5
Hydrogen (ASTM D5991)	*[mol%]*	~13.5
Oxygen (ASTM D5991)	*[mol%]*	~1.4

The absolute intake air pressure and temperature were 1.42 bar and 50°C, respectively. The in-cylinder temperature and density at the TDC in motored conditions were 812°C and 20.2 kg/m^3, respectively. The injection strategies consisted of two events per cycle, pilot and main; the injection pressure was set to 891 bar. Commercial diesel fuel has been used and its properties have been reported in Table 3.

3 Results and discussion

Figure 2 reports the combustion macroscopic signals as the in-cylinder pressure, the calculated rate of heat release (ROHR), and the injector current for the real engine (dashed line) and for the derived optical engine (solid line with symbols). The solenoid current signals are the same for both engines since the same injection strategies have been performed.

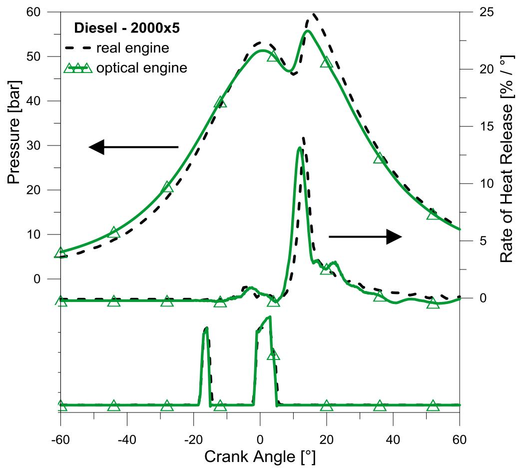

Fig. 2 In-cylinder pressure, ROHR and injector current for diesel fuel at 2000x5 in both real and optical engines

The pressure value at 0°CA that is the top dead center (TDC) in the optical engine is close to the real engine one. The main target was to overlap the ROHR trace in order to reproduce the same combustion behavior [16, 19]. Figure 2 shows a good fit of the ROHR curves of real and optical engines. By managing the intake temperatures, it was possible to match the start of combustion (SOC) of the optical engine with the real engine one. The SOC has been detected as the instant when the energy release begins to exceed the energy losses due to the fuel evaporating process [20]. The SOC of the pilot and main injections occur at -9°CA and 5°CA. The combustion of the pilot injection releases a small quantity of energy; it generates a local peak with low intensity. On the other hand, the combustion of the main injection releases the main energy and it is characterized by a fast increase of heat release typical of premixed combustion. Finally, optical engine demonstrated to reproduce the combustion cycle of the real engine in a reliable way and this is mandatory for the analysis of in-cylinder processes by means of optical diagnostics.

In addition to the analysis of in-cylinder signals, optical engines give the advantage to obtain information about the combustion process through the direct visualization of the phenomena that take place inside the cylinder. 2d imaging during the injection and combustion phases has been performed and in Figure 3 visible images have been shown for the tested operating condition. The images of the combustion flames have been reported from the TDC to 20°CA. The natural luminosity flames can be detected starting from the TDC (indicated as Start of visible combustion in Figure 3); these flames are due to the pilot combustion because the main SOC occurs later, at 5°CA. The reactions that take place immediately after the SOC of the pilot cannot be detected in the visible range and this is a limitation of the optical diagnostic in the visible spectrum. After the start of visible combustion, the in-cylinder reactions continue and the flames are visible also during the main injection event (from 4°CA to 10°CA). At 10°CA, part of the fuel of the main injection start to ignite. However, due to the short time available to mix with the air, this combustion is rich in fuel and the flames intensity is very high. After the end of injection, 12°CA, the flames are located mainly on the jets axes and spread on the chamber wall. In the following images (from 14°CA to 20°CA), the flames form a ring on the periphery of the combustion chamber. This indicates that fuel is available in that location even though there is no evidence of the fuel reaching the chamber wall from visible imaging of the injection process.

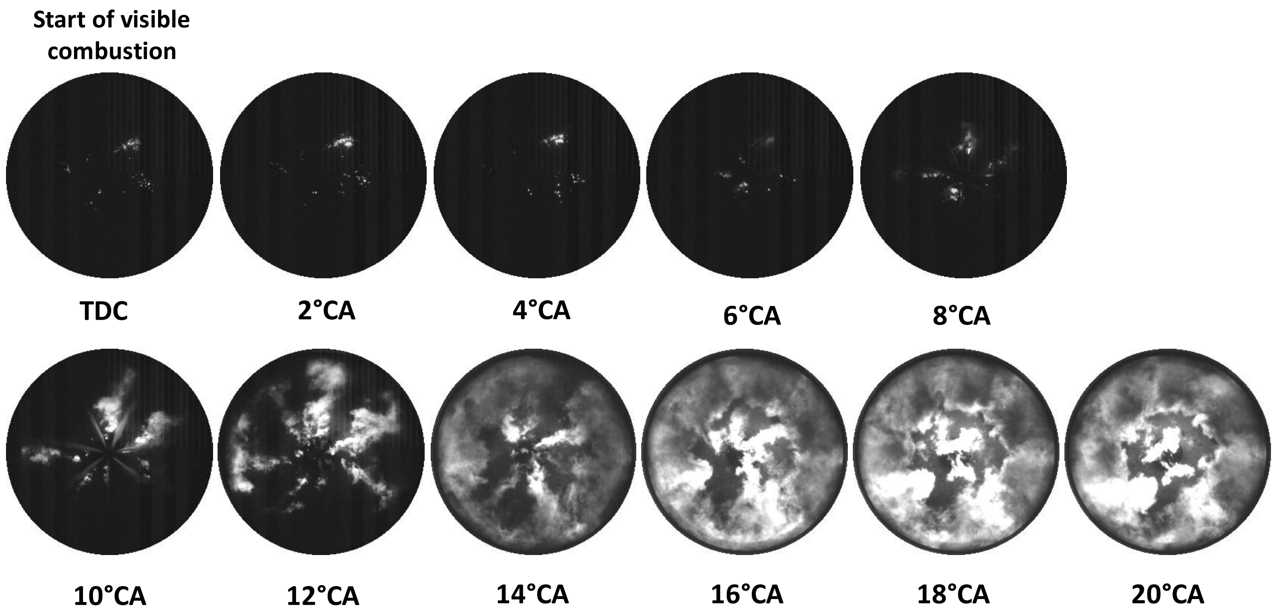

Fig. 3 Images of the main injection and combustion evolution in the visible spectrum

Figure 4 reports a collection of images of the injection and combustion processes in the full infrared range of the camera that is from 1.5 to 5 µm. Half of the actual field of view has been selected in order to reach an image temporal resolution of 2°CA. The upper part of the combustion chamber is visualized and the two intake valves are visible, the injector tip is in the center of the bottom side of the images. Different color-scale limits have been used to get the best visualization for each image. Further images than figure 3 have been reported from -14°CA to the TDC the show the injection, the diffusion, and the reaction of the pilot injection. Previous works [21] pointed out that the visible imaging was not able to detect the evaporated fuel and the low temperature reactions after the end of pilot injection and before the start of luminous combustion. On the contrary, in the infrared band, the fuel spreading from the nozzle toward the chamber wall can be easily detected. In Figure 4, more intense emissions are evident since -6°CA that is before the start of luminous combustion (TDC). Infrared imaging in the full spectrum of the camera is able to follow the in-cylinder reactions (from 4°CA to 4°CA) but those superimpose on the main injection that is no longer detectable (from 4°CA to 10°CA). However, the strength of the reactions that are occurring during the main injection event is well caught by this technique. After 14°CA the detector is saturated by the flames intensity.

To highlight the fuel distribution in the combustion chamber a band pass filter has been used to collect the infrared emission in a narrow band centered at 3.9 µm. This wavelength cuts the emissions from the hot gases that cover the jets and highlights the hydrocarbons emissions. In Figure 5, the images at 3.9 µm have been reported. Differently from the previous case, during the pilot injection, the fuel is visible only at -12°CA while in the following crank angles there are only weak ghosts not clearly detectable. The strong radiation of the luminous combustion can be detected also at this wavelength and it is visible from the TDC to 2°CA. From 4°CA to 12°CA, the main injection event can be visualized and additional information with respect to visible images have been obtained. At 4°CA and 6°CA, similar jet shapes can be observed between figures 3 and 5; on the contrary, at 8°CA, the jet is wider in the infrared. This is due to the sensitivity of the infrared detector to both regions with high fuel concentrations (jet core) and high air/fuel mixing temperature (jet periphery) [22]. Further significant observations concern the images at 10°CA and 12°CA where the fuel impingement on the chamber wall is evident. After reaching the wall, the fuel spreads laterally and the jet tips assume a mushroom shape. At 12°CA some interactions between the adjacent jets can be observed. From 14°CA on, the flame propagation in the combustion chamber is evident.

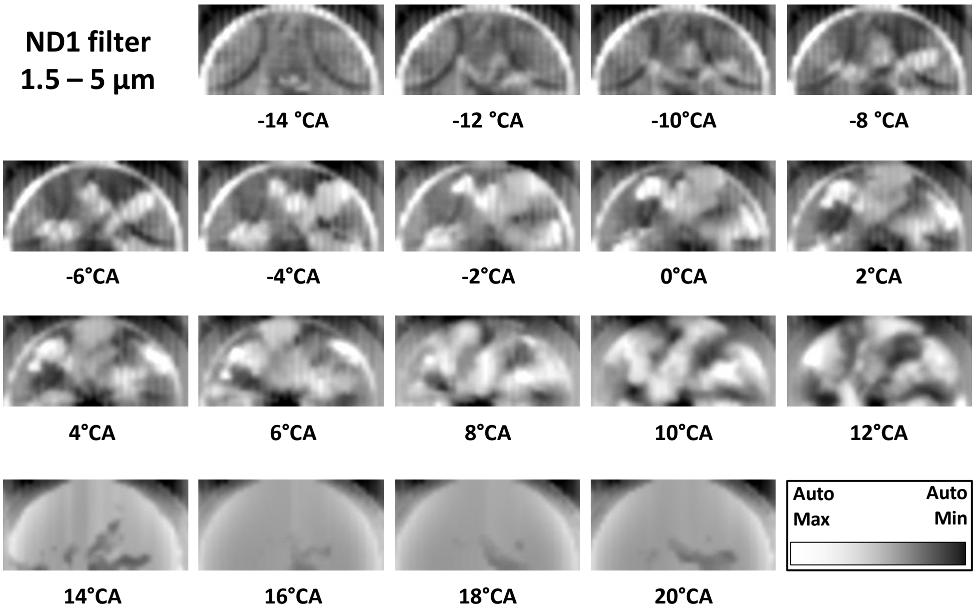

Fig. 4 Images of the main injection and combustion evolution in the full infrared range

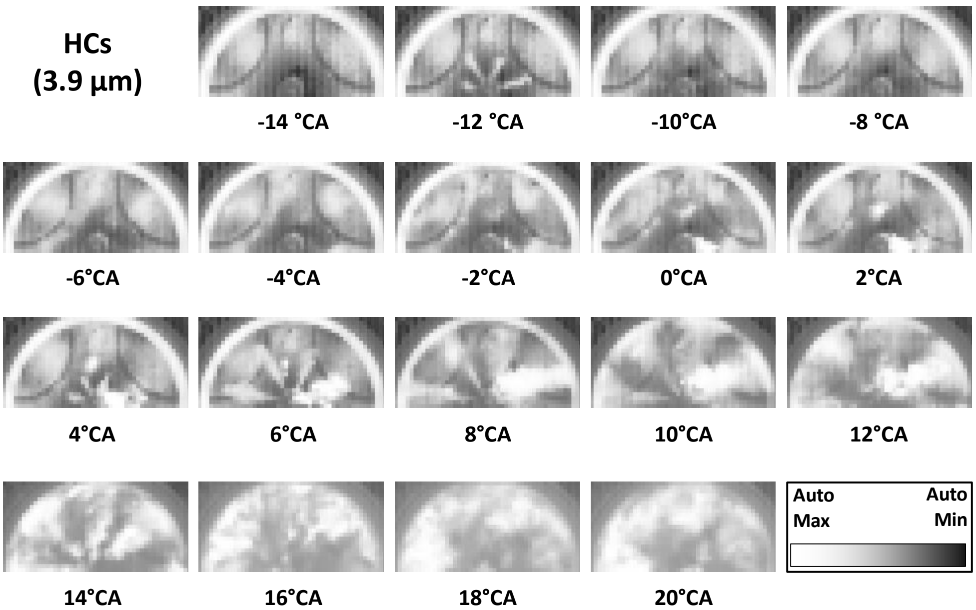

Fig. 5 Images of the main injection and combustion evolution at 3.9 µm

Another interesting species to trace in the infrared spectrum is the CO_2 molecule that has at 4.2 µm its asymmetric stretch vibration mode. Images recorded at this wavelength using a band pass filter have been reported in Figure 6 for the same crank angles of figures 4 and 5. The images show that CO_2 is detectable even during the compression phase since this engine is performing real exhaust gas recirculation. No significant variations of CO_2 emissions have been observed during this phase; moreover it is almost homogeneously distributed in the whole combustion chamber. The main comments concern the period when the fuel reaches the chamber wall (8°CA – 12°CA, see Figure 5); in this case, separated clouds of CO_2 are formed close to the wall in correspondence of the points where the jets impinge. The presence of these clouds affect the following stage, that is when the luminous combustion take place (see Figure 3), producing a ring shaped CO_2 distribution that is similar to the one of the visible flames (Figure 3).

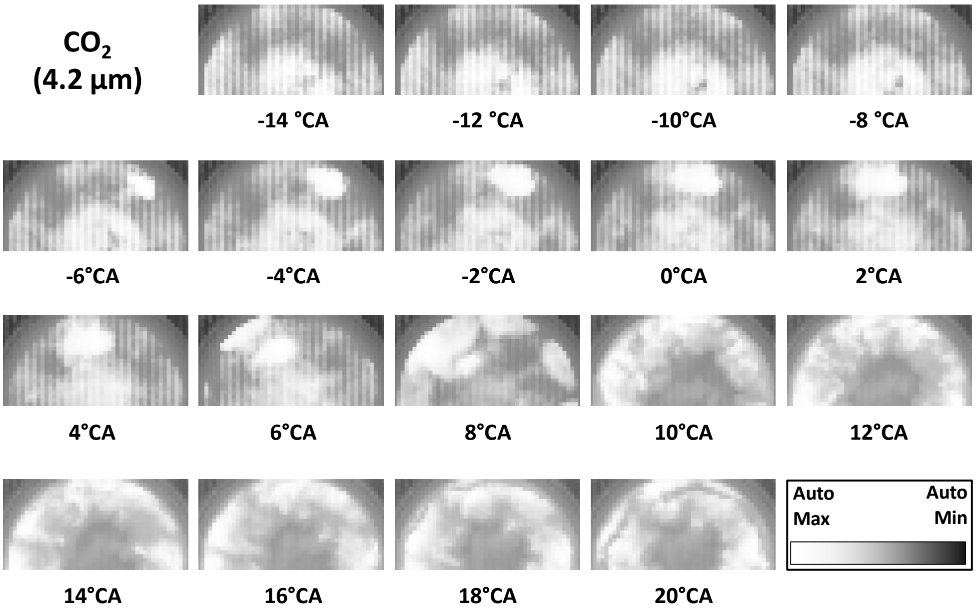

Fig. 6 Images of the main injection and combustion evolution at 4.2 µm

Currently, the availability of infrared cameras is very low and they are typically not designed for such high-speed applications as diagnostics in internal combustion engines. For this reason, often one image per cycle is recorded and then all the images are collected together to obtain an approximated behavior of combustion process. On the other hand, the advantage of using a cycle resolved camera, as in this work, is that all the recorded images belong to the same combustion event and subsequent repetitions of the combustion cycle can be acquired in order to get a statistical behavior. Each recorded image can be considered as a matrix where the value of each cell is the corresponding pixel digital level (DL). Considering one image at a certain crank angle, the average value of the image is the sum of all the values of each cell divided for the cell number. This procedure obtains one number from each image; then, applying it to all the recorded images, a curve of average pixel values versus crank angle can be obtained. In particular, there will be as many curves as the subsequent recorded cycles. In Figure 7, an example of the infrared emission curves calculated from the images in the full infrared camera range across 24 subsequent repetitions have been reported. The data dispersion of the curves can be noted. To carry out a statistical analysis of the combustion behavior and to investigate the sensitivity of the two techniques and different optical configurations, the ensemble-averaged curve and the standard deviation curve for each configuration have been calculated. Figure 8 reports the mean (solid line) and the standard deviation (dashed line) curves for the visible images and the infrared in the full camera range, at 3.9 µm and at 4.2 µm. Moreover, the in-cylinder pressure and the rate of heat release (ROHR) have been reported to follow the evolution of the combustion process. Generally, for all the optical configurations, the radiation from the combustion chamber starts to increase in the range 7-10°CA; before for the infrared images (7°CA) due to the higher sensitivity to vapor and low temperature reactions, and later for the visible ones (10°CA). The curves are characterized by different decreasing slopes; in particular, in the band 1.5 – 5 µm and at 4.2 µm, lower slopes have been noted and the emitted radiation is very strong also during the late combustion phase (after 50°CA). On the other hand, the visible radiation curve and the one at 3.9 µm have similar shapes. It is very interesting to observe that in all the cases the standard deviation curve has the same behavior. Low data dispersions around the TDC are followed by a peak of standard deviation and finally the curves return to low values after more or less intense oscillations. The peak of standard deviation is reached for all the case at the same time and it corresponds to the crank angles when the fuel of the main injection burns in rich condition, as stated before. The presence of reactants in the proper concentration for the start of combustion is not the same each cycle and this causes the high data dispersion observed. The closeness of the peaks of all the curves indicates that the infrared imaging is a suitable technique to investigate the evolution of luminous flames. Moreover, this technique is also robust as the same behavior has been observed in the full camera range and with two band pass filters.

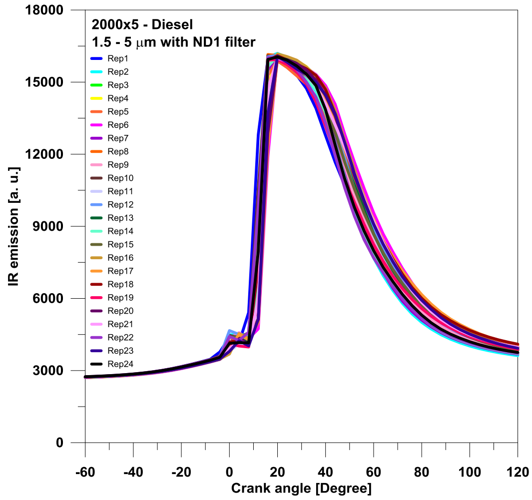

Fig. 7 Emission curves in full infrared range for 24 subsequent repetitions of the combustion process

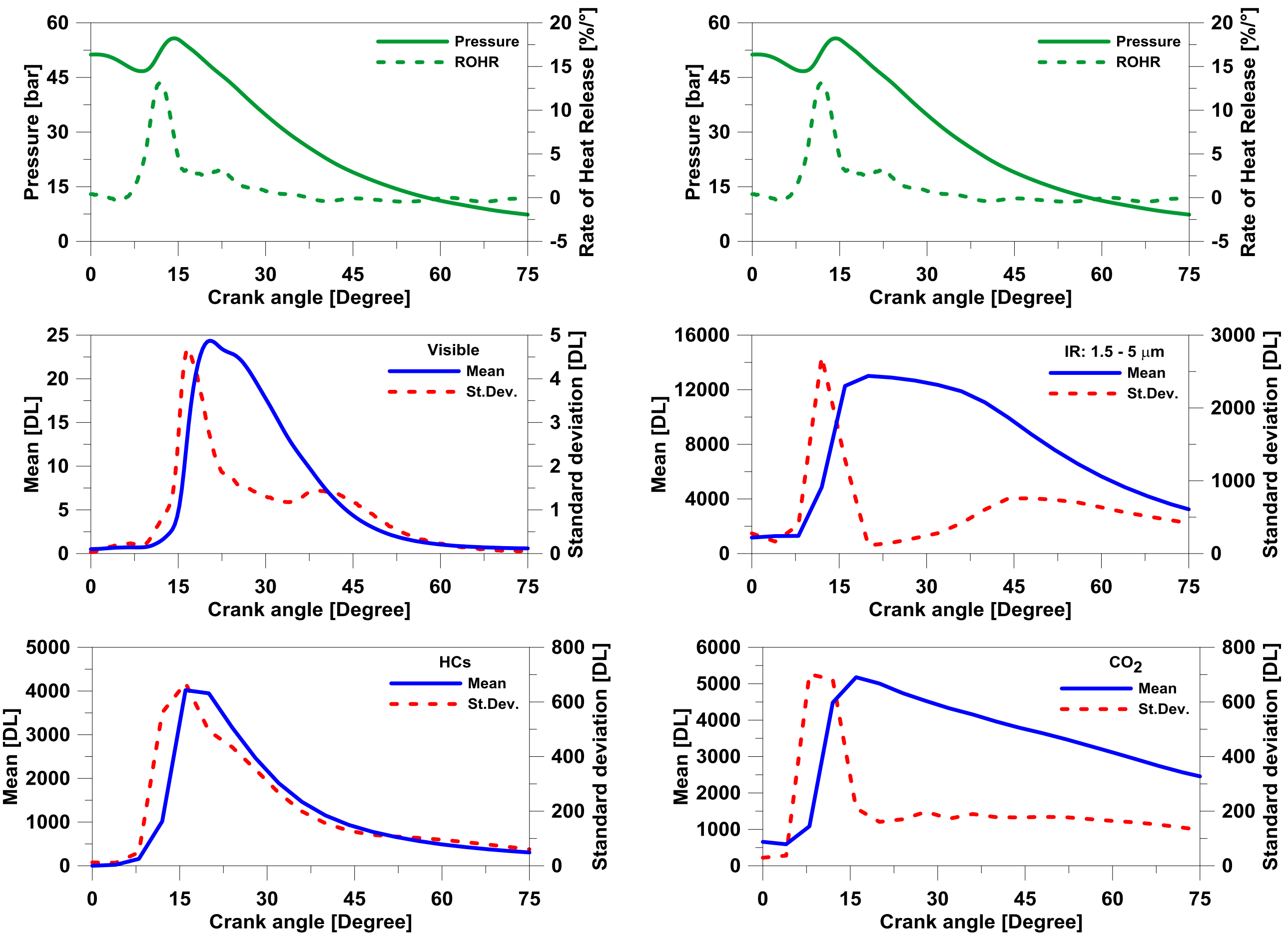

Fig. 8 In-cylinder pressure, ROHR, and calculated emission curves (Mean and Standard Deviation) for the images in the visible, full infrared range, and at 3.9 μm and at 4.2 μm

Due to the different absolute values of the standard deviation curves, the graphs in Figure 8 do not give any useful indication about the extent of the data dispersion for each configuration. They span from 3000 DL for the full infrared spectrum to 5 DL for the visible images. For this reason, the coefficient of variation (CV), that is the ratio between the standard deviation and the mean value, has been calculated for each case of

Figure 8. Curves of CV versus crank angle have been reported in Figure 9. The results shown in Figure 9 are very interesting and they are not available in previous literature. For all the investigated configurations, the CV spans in the same range during the whole combustion period. The peak value is at 12°CA for the visible, infrared band 1.5 – 5 µm, and at 3.9 µm while it is at 8°CA for the curve at 4.2 µm. The peak value is around 0.55 while it decreases to 0.1-0.2 in the late combustion phase. The agreement of the curves of figure 9 indicates that the infrared technique can be used to follow the cycle-to-cycle dispersion without putting in the measure any additional error.

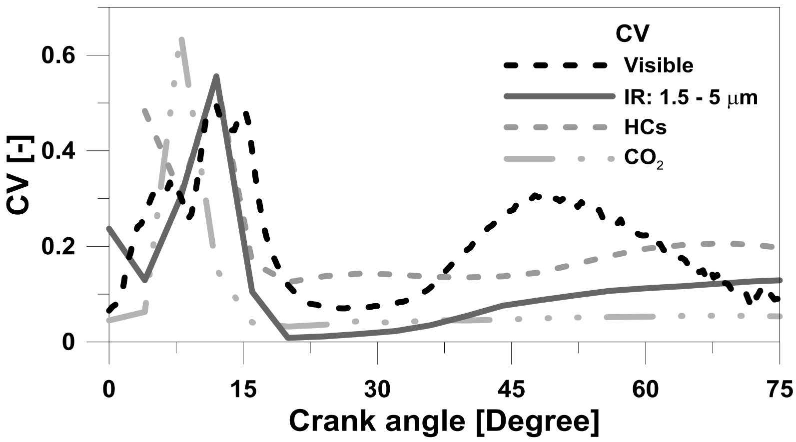

Fig. 9 Curves of the Coefficient of Variation (CV) calculated from the emission curves of figure 8

After a macroscopic analysis of the cycle-to-cycle variation based on the emitted radiation from the combustion chamber in the visible and infrared spectrum, the crank angle with the maximum data dispersion has been identified, it is during the early combustion phase, at 12°CA for most of cases. However, beside the time of the maximum CV it would be interesting to analyze also its position in the combustion chamber. To this aim, all the images at 12°CA of different repetitions have been collected and, for each pixel position, the standard deviation has been calculated and plotted as an image. The post-processed images for the four cases, at 12°CA, have been shown in Figure 10 (half view of the combustion chamber has been selected also for the visible image in order to simplify the comparison). Despite of the final considerations made for Figure 9, where all the optical configurations could detect the instant of maximum data dispersion, in the terms of spatial position different locations in the combustion chamber will be pointed out according to the technique used. This is a great benefit because more than one critical process can be identified and fixed. Briefly, the visible images denote low dispersion of the flames close to the wall, where more fuel is available, and high dispersion in the center of the chamber. At 3.9 µm, since the HCs are detected, the maximum data dispersion is located along the jets axes. According to the ring shape of the CO_2 emission, also the data dispersion at 4.2 µm is characterized by the same profile with very low values in the center of the combustion chamber. Finally, very low and homogeneous values of standard deviation have been calculated for the image in the full infrared camera range.

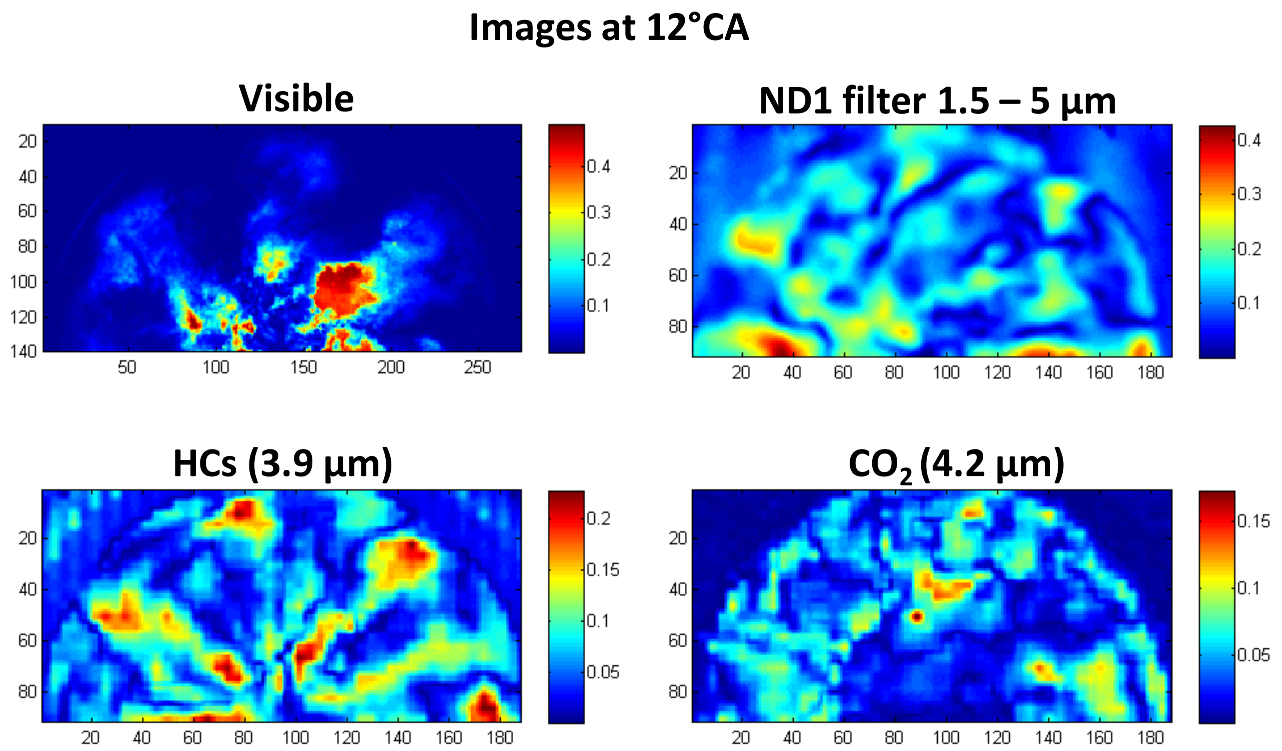

Fig. 10 2d visualization of the image standard deviation at 12°CA for all the optical configurations

4 Conclusions

In this work, 2d infrared imaging is performed in order to analyze the mixing process in a diesel engine. In-cylinder images have been acquired using two high speed cycle resolved cameras, one for the visible and one for the IR spectrum. The infrared range investigated is from 1.5 to 5 µm; moreover a band pass filter at 4.2 µm has been used to impress the radiation of the CO_2 molecules while one at 3.9 µm for the detection of HCs.

In the infrared range, the injection, the diffusion, and the reaction of the pilot injection have been visualized. For the main injection, the fuel impingement on the chamber wall, the lateral diffusion, and the interactions between the adjacent jets have been observed. Wider and more accurate jet boundaries have been detected due to the high sensitivity of the infrared detector to both high concentrations and high mixing temperature regions. CO_2 has been detectable during the compression phase and it is almost homogeneously distributed. Then, CO_2 clusters are formed close to the wall in correspondence of the points where the jets impinge.
The statistical analysis of the cycle-to-cycle variation has demonstrated that in all the cases the standard deviation curves have the same behavior. The peak of standard deviation is reached for all the case at the same time that is when rich combustion occurs.
The data dispersion in terms of CV is the same for all the configurations used, no additional error are added using infrared imaging. The analysis of the spatial data dispersion has pointed out that different critical locations can be identified according to the technique used.
The availability of additional insights on the combustion process and the agreement between the cycle-to-cycle variation results indicate that the infrared imaging is a suitable technique to investigate the behavior of internal combustion engines.

References

[1] Leipertz A, Wensing M, (2007) Modern optical diagnostics in engine research. *Journal of Physics: Conference Series*, vol. 85, no. 1, p. 012001.

[2] Settles G, (2001) Schlieren and Shadowgraph Techniques: Visualizing Phenomena in Transparent Media. Springer.

[3] Zhao H, (2012) Laser Diagnostics and Optical Measurement Techniques in Internal Combustion Engines.

[4] Zhao H, Ladommatos N, (2001) Engine combustion instrumentation and diagnostics, Warrendale, PA: Society of Automotive Engineers, pp 842, 2001.

[5] Jansons M, Lin S, Rhee K, (2008) Infrared spectral analysis of engine preflame emission, *International Journal of Engine Research*, vol. 9, no. 3, pp. 215–237.

[6] Dombrovsky L, Sazhin S, Mikhalovsky S, Wood R, Heikal M R, (2003) Spectral properties of diesel fuel droplets, *Fuel*, vol. 82, no. 1, pp. 15–22.

[7] Trujillo E C, Jiménez-Espadafor F J, Villanueva J A B, Garcá M T, (2011) Methodology for the estimation of cylinder inner surface temperature in an air-cooled engine, *Applied Thermal Engineering*, vol. 31, no. 8, pp. 1474–1481.

[8] Royo R, Albertos-Arranz M, Cárcel-Cubas J, Payá J, (2012) Thermographic study of the preheating plugs in diesel engines, *Applied Thermal Engineering*, vol. 37, pp. 412–419.

[9] Royo R, (2004) Characterization of automotion brake thermal conditions by the use of infrared thermography, *Infrared Training Center and FLIR Systems*, pp. 259–266.

[10] Royo R, (2003) Characterization of the exhaust flow in the catalytic converter of a spark ignition engine using infrared thermography, *The Infrared Training Center*, pp. 192–200.

[11] Mancaruso E, Sequino L, Vaglieco B M, (2011) IR imaging of premixed combustion in a transparent Euro5 diesel engine, *SAE Technical Paper 2011-24-0043*, doi:10.4271/2011-24-0043.

[12] Mancaruso E, Sequino L, Vaglieco B M, (2013) GTL (Gas To Liquid) and RME (Rapeseed Methyl Ester) combustion analysis in a transparent CI (compression ignition) engine by means of IR (infrared) digital imaging, *Energy*, vol. 58, pp. 185–191.

[13] Mancaruso E, Sequino L, Vaglieco B M, (2014) IR digital imaging for analysing in-cylinder combustion process in transparent diesel engine. In: Photonics Technologies, 2014 Fotonica AEIT Italian Conference on. IEEE, pp. 1–4.

[14] Pecsok R L, Shields L D, (1968) Modern Methods of Chemical Analysis, Wiley, New York.

[15] Pavia D, Lampman G, Kriz G, Vyvyan J, (2008) Introduction to spectroscopy. Cengage Learning.

[16] Aronsson U, Chartier C, Horn U, Andersson Ö, Johansson B, and Egnell R, (2008) Heat release comparison between optical and all-metal HSDI diesel engines," *SAE Technical Paper 2008-01-1062,* doi:10.4271/2008-01-1062, .

[17] Colban W F, Kim D, Miles P C, Oh S, Opat R, Krieger R, Foster D, Durrett R P et al., (2009) A detailed comparison of emissions and combustion performance between optical and metal single-cylinder

diesel engines at low temperature combustion conditions, *SAE International Journal of Fuels and Lubricants*, vol. 1, no. 1, pp. 505–519.

[18] Heywood J B, (1988) Internal combustion engine fundamentals. McGraw-Hill New York, vol. 930.

[19] Aronsson U, Solaka H, Lequien G, Andersson Ö, Johansson B, (2012) Analysis of errors in heat release calculations due to distortion of the in-cylinder volume trace from mechanical deformation in optical diesel engines, *SAE International Journal of Engines*, vol. 5, no. 4, pp. 1561–1570.

[20] Karinen R, Krause A, (2006) New biocomponents from glycerol, *Applied Catalysis A: General*, vol. 306, pp. 128–133, .

[21] Mancaruso E, Vaglieco B M, Sequino L, (2015) Using 2d Infrared Imaging for the Analysis of Non-Conventional Fuels Combustion in a Diesel Engine, *SAE Int. J. Engines* 8(4):2015, doi:10.4271/2015-01-1646.

[22] Eagle W E, Malbec L M, Musculus M P B, (2015) Comparing Vapor Penetration Measurements from IR Thermography of C-H Stretch with Schlieren during Fuel Injection in a Heavy-Duty Diesel Engine, In: 9th U. S. National Combustion Meeting, May 17-20, Cincinnati, Ohio.